Inorganic Chemistry

pubs.acs.org/IC

Article

Polar Structure and Two-Dimensional Heisenberg Antiferromagnetic Properties of Arylamine-Based Manganese Chloride Layered Organic–Inorganic Perovskites

Liany Septiany, Diana Tulip, Mikhail Chislov, Jacob Baas, and Graeme R. Blake*

Cite This: *Inorg. Chem.* 2021, 60, 15151–15158

Read Online

ACCESS | Metrics & More | Article Recommendations | Supporting Information

ABSTRACT: The breaking of inversion symmetry can enhance the multifunctional properties of layered hybrid organic–inorganic perovskites. However, the mechanisms by which inversion symmetry can be broken are not well-understood. Here, we study a series of $MnCl_4$-based 2D perovskites with arylamine cations, namely, $(C_6H_5C_xH_{2x}NH_3)_2MnCl_4$ (x = 0, 1, 2, 3), for which the x = 0, 1, and 3 members are reported for the first time. The compounds with x = 1, 2, and 3 adopt polar crystal structures to well above room temperature. We argue that the inversion symmetry breaking in these compounds is related to the rotational degree of freedom of the organic cations, which determine the hydrogen bonding pattern that links the organic and inorganic layers. We show that the tilting of $MnCl_6$ octahedra is not the primary mechanism involved in inversion symmetry breaking in these materials. All four compounds show 2D Heisenberg antiferromagnetic behavior. A ferromagnetic component develops in each case below the long-range magnetic ordering temperature of ∼42–46 K due to spin canting.

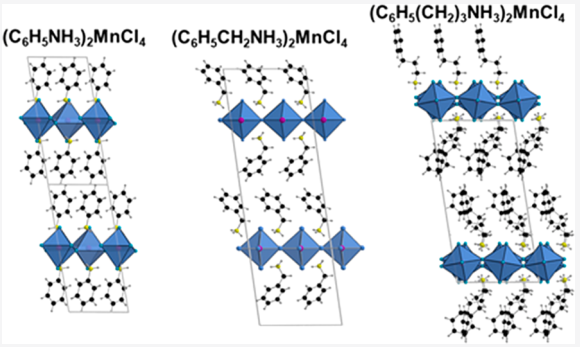

INTRODUCTION

Two-dimensional (2D) inorganic–organic halide perovskites containing lead and tin have in recent years been studied intensively in the context of their excellent photovoltaic and optoelectronic properties.[1−5] If lead or tin is replaced by a transition metal, 2D perovskites can also exhibit interesting magnetic properties. Such materials have been known since the 1970s as model systems for the study of 2D magnetism,[6] and very recently as potentially useful materials in magnetocaloric cooling applications.[7,8] It might be possible to further extend the utility of hybrid perovskites to a wider range of energy storage and conversion technologies including thermoelectric waste heat harvesting, capacitors, and batteries.[9]

Compared to their 3D analogues, 2D halide perovskites tend to have better stability with respect to degradation under ambient conditions and are more versatile with respect to the organic cations that can be incorporated. The crystal structure generally consists of inorganic layers, usually in the form of corner-shared metal halide octahedra, which are separated by bilayers of the organic cation (see Figure 1). The two blocks are connected by hydrogen bonding between the protons of the ammonium group and the halide anions. The corner-shared octahedral network in the inorganic layers is often distorted. The voids between adjacent octahedra are occupied by the ammonium group of the organic cation, which may have different conformations related to the length of the alkyl tail.

Although most 2D hybrid perovskites are reported to adopt centrosymmetric crystal structures, it has been proposed that their functionality with respect to many of the applications mentioned above can be enhanced if inversion symmetry is broken, as summarized in several recent reviews.[9−11] For example, a polar structure might lead to longer carrier lifetimes in photovoltaic materials, enhancing the separation and collection of charges.[10] Polar structures containing magnetic cations lead to the prospect of coexisting ferroelectric and magnetic order, which can potentially lead to improved electronic devices and data storage technology.[12−14]

For 2D perovskites, a number of reports suggest that the incorporation of arylamine-based organic cations between the inorganic layers can result in a polar structure at room temperature. Such cations have flexible alkyl-ammonium tails and rigid phenyl rings and can be used to introduce more distortion to the structure. For example, $(C_6H_5C_2H_4NH_3)_2CuCl_4$ and $(C_6H_5C_4H_8NH_3)_2CuCl_4$ are reported to exhibit simultaneous electrical polarization and magnetic ordering.[15,16] In the former, it is thought that either a

Received: May 17, 2021
Published: September 27, 2021

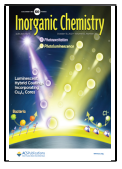

https://doi.org/10.1021/acs.inorgchem.1c01011
Inorg. Chem. 2021, 60, 15151–15158

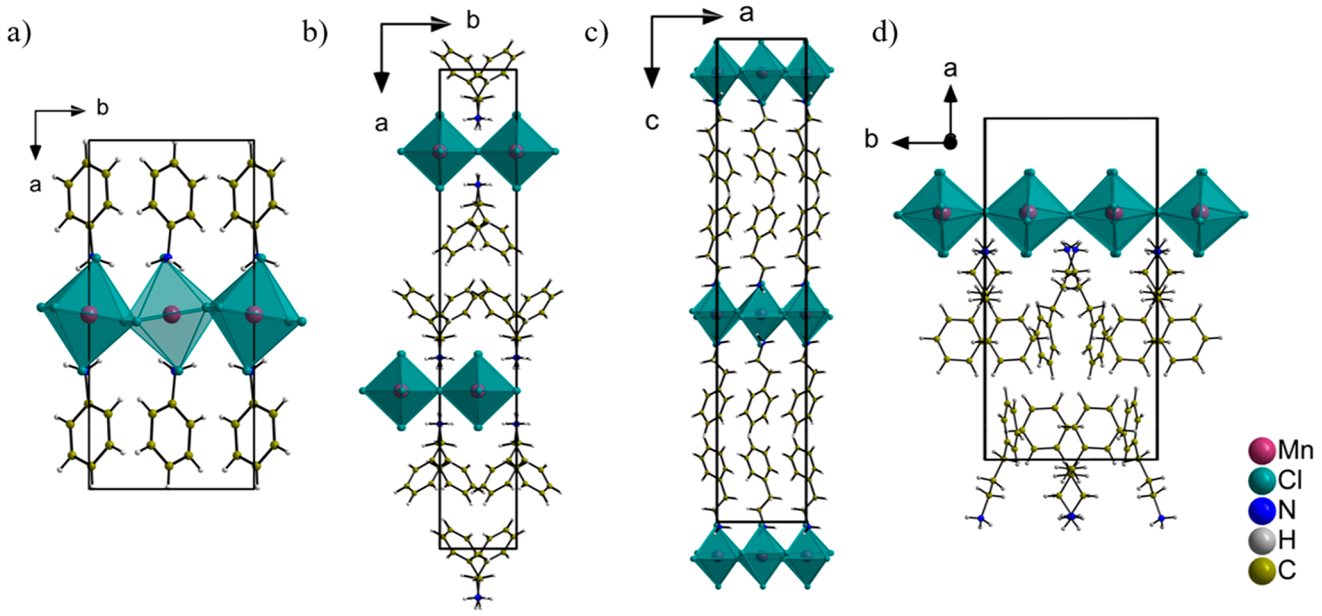

Figure 1. Crystal structures of (a) $(PA)_2MnCl_4$, (b) $(PMA)_2MnCl_4$, (c) $(PEA)_2MnCl_4$, and (d) $(PPA)_2MnCl_4$ at 100 K.

slight tilt of the organic cation breaks inversion symmetry, or that an order−disorder transition involving hydrogen bonding configurations is responsible. In the latter, the mechanism is also thought to involve hydrogen bond ordering. We note that it is often challenging to assign the correct space group during structure determination. For example, Kamminga et al. found that $(C_6H_5C_2H_4NH_3)_2MnCl_4$ has a polar structure at room temperature after a detailed structural analysis, whereas the same compound was previously assigned to a centrosymmetric space group.[17] There are as yet no conclusive guidelines as to which structural features lead to inversion symmetry breaking or to the mechanisms by which this can occur. Therefore, there is a need to study more examples of polar 2D halide perovskites and to understand how and why inversion symmetry can be broken. Here we present the structure of three novel $MnCl_4$-based layered perovskites, by which we show that with sufficient alkyl-ammonium tail length a polar structure can be obtained at room temperature.

Regarding the magnetic properties of 2D hybrid perovskites, since the metal halide layers are often separated by more than 1 nm, they tend to behave as quasi-2D Heisenberg magnets. Depending on the metal cations used in the inorganic layer, they can exhibit ferromagnetic ordering (Cu^{2+})[15,16,18−20] or antiferromagnetic ordering (Mn^{2+} and Fe^{2+}).[21−26] In previous studies, 2D $MnCl_4$-based perovskites were shown to undergo long-range antiferromagnetic ordering below temperatures varying from 39 to 47 K.[21−24] Although an ideal 2D Heisenberg magnet does not undergo ordering at any finite temperature,[27] it may still occur due to Ising anisotropy or the Dzyaloshinsky−Moriya (DM) interaction.[22] Lee et al. reported that the ordering temperature in 2D $MnCl_4$-based perovskites decreases with an increasing length of the organic cations for straight alkylammonium chains (C1−C4) until a lowest value of ∼43 K is reached,[22] due to a decrease in the interlayer exchange interaction as the distance increases. However, as the length of the cation increases beyond 8 carbon atoms, the superexchange interaction alone cannot describe the trend in transition temperature as the relative influence of Ising anisotropy and DM interactions become more pronounced. Park et al. reported canted antiferromagnetism for single crystals of $(C_6H_5C_2H_4NH_3)_2MnCl_4$, where the spin canting was observed in low applied magnetic field below the magnetic ordering temperature[21] and the magnetization showed significant anisotropy between the in-plane and out-of-plane directions. The easy-axis was claimed to lie along the layer stacking direction.

In this study, we discuss the effect of organic cation length on the breaking of inversion symmetry and on the magnetic properties of 2D $MnCl_4$-based perovskites. We use four different arylamine-based organic cations, namely, phenylamine (also referred to as aniline, $C_6H_5NH_3$), phenylmethylamine (benzylamine, $C_6H_5CH_2NH_3$), phenylethylamine (phenethylamine, $C_6H_5C_2H_4NH_3$), and phenylpropylamine ($C_6H_5C_3H_6NH_3$). We find that only $(C_6H_5NH_3)_2MnCl_4$ crystallizes in a centrosymmetric structure, while the others adopt polar structures from 100 K to above room temperature. All four compounds show 2D antiferromagnetism with transitions to a canted, long-range ordered state below 42−46 K.

EXPERIMENTAL SECTION

Crystal Growth. Aniline hydrochloride (Sigma-Aldrich; 97%), benzylamine (Sigma-Aldrich, 99%), 2-phenethylamine hydrochloride (Sigma-Aldrich; ≥98%), and 3-phenyl-1-propylamine (Sigma-Aldrich; 98%) were used as the arylammonium source. Salts of phenylmethylammonium and phenylpropylammonium chloride were synthesized by mixing the organic liquid with HCl (Sigma-Aldrich; 2.5 M in EtOH) in ethanol absolute, resulting in a white powder. The powder was then washed with diethyl ether (Macron Chemicals) and vacuum-dried overnight.

A 1:2 molar ratio of $MnCl_2$ (Sigma-Aldrich; ≥99%) and the respective arylammonium chloride salt was dissolved in absolute ethanol. Single crystals were grown by slow evaporation of the solvent at 60 °C. After ∼1 week, single crystals were obtained from solution as platelets with different colors depending on the organic cation used.

X-ray Diffraction. Single-crystal X-ray diffraction (XRD) measurements were carried out using a Bruker D8 Venture diffractometer operating with Mo Kα radiation, equipped with a Photon 100 area detector and a Triumph monochromator. The crystals were placed on a glass fiber using a commercial acrylate glue

https://doi.org/10.1021/acs.inorgchem.1c01011
Inorg. Chem. 2021, 60, 15151−15158

Table 1. Structural Parameters of $(PA)_2MnCl_4$, $(PMA)_2MnCl_4$, $(PEA)_2MnCl_4$, and $(PPA)_2MnCl_4$ at 100 K

	$(PA)_2MnCl_4$	$(PMA)_2MnCl_4$	$(PEA)_2MnCl_4$	$(PPA)_2MnCl_4$
organic cation	phenylammonium ($C_6H_5NH_3$)	phenylmethylammonium ($C_6H_5CH_2NH_3$)	phenylethylammonium ($C_6H_5CH_2CH_2NH_3$)	phenylpropylammonium ($C_6H_5CH_2CH_2CH_2NH_3$)
MW (g/mol)	385.01	413.07	441.12	469.18
space group	$P2_1/c$, centrosymmetric	Cc, polar	$Pca2_1$, polar	Pc, polar
a (Å)	15.3747(11)	32.496(5)	7.2352(10)	20.6463(21)
b (Å)	7.1706(5)	5.1630(8)	7.1390(10)	10.3297(11)
c (Å)	7.1112(5)	10.3195(14)	39.028(6)	10.3353(10)
β (deg)	99.543(3)	97.873(6)	90.000	98.783(5)
V (Å^3)	773.13(9)	1715.0(4)	2015.9(5)	2178.4(4)
Z	2	4	4	4
density (g/cm^3)	1.654	1.600	1.453	1.431
GOF	0.795	1.145	1.249	1.047
R1	0.0417	0.0969	0.0852	0.1173
largest diff. peak/hole (e/Å^3)	0.47/−0.39	1.30/−0.93	1.77/−1.89	2.12/−1.07

for measurements above room temperature, while for low-temperature measurement the crystals were mounted on a nylon fiber loop using cryo-oil. An Oxford Cryostream Plus with dry nitrogen flow was used to regulate the measurement temperature. The data obtained were processed using the Bruker APEX III software. Structures were solved by direct methods, and refinement was carried out using the SHELX97 software.[28]

For powder XRD measurement at room temperature, the crystals were hand-ground into a fine powder using an agate mortar and pestle. The measurements were carried out using a Bruker D8 Advance diffractometer equipped with a Cu−Kα source. The structural parameters were determined by Rietveld refinement using the GSAS software.[29]

Magnetic Measurement. Magnetic measurements were carried out using a Quantum Design MPMS SQUID magnetometer. The single crystals, all in the form of platelets, were measured with the applied field along the in-plane and out-of-plane directions. The temperature dependence of the DC magnetization was measured on warming from 5 to 300 K after field cooling in 1000 Oe. Measurements of magnetization versus applied field were carried out up to 6 T at different temperatures, after cooling in zero magnetic field.

RESULTS AND DISCUSSION

The crystal structures of $(C_6H_5NH_3)_2MnCl_4$ [$(PA)_2MnCl_4$/**1**], $(C_6H_5CH_2NH_3)_2MnCl_4$ [$(PMA)_2MnCl_4$/**2**], and $(C_6H_5C_3H_6NH_3)_2MnCl_4$ [$(PPA)_2MnCl_4$/**4**] have not previously been reported, whereas the n = 2 compound $(C_6H_5C_2H_4NH_3)_2MnCl_4$ [$(PEA)_2MnCl_4$/**3**] has been studied previously;[14] the structure of our current crystals of **3** is consistent with the earlier report. The structures of **1**−**4** determined at 100 K are presented in Figure 1a−d. Compound **1** crystallizes in a centrosymmetric (nonpolar) space group whereas **2**, **3**, and **4** have polar structures. The structural parameters are listed in Table 1. We note that it is often difficult to identify the breaking of inversion symmetry by diffraction methods.[15] However, for **2** and **4** we attempted structure solution in the corresponding centrosymmetric space groups ($C2/c$ and $P2/c$, respectively) and could not obtain satisfactory structural models.

We observe broken inversion symmetry when the organic cation has an alkyl chain of at least one carbon atom. To compare, 2D $MnCl_4$-based perovskites adopt centrosymmetric structures when the cation has a simple alkyl chain.[30−33] This implies that the introduction of a phenyl ring can lead to a polar structure. It is therefore useful to examine the structures of **1**−**4** in more detail to identify the mechanism by which inversion symmetry is broken.

It was previously reported that the onset of a polar phase for **3** involves the opening of a small dihedral angle between the phenyl rings of adjacent PEA molecules, which are crystallographically distinct.[17] The rotation of the phenyl rings also induces a change in the bond angles and hence lengths of the alkyl ammonium tails of the PEA molecules. This difference gives rise to an asymmetric approach of the organic cations to the inorganic layer, inducing different hydrogen bond lengths associated with the two molecules, which also shifts the Mn^{2+} away from the center of the octahedron. With an increasing number of carbon atoms in the alkyl ammonium tail of the organic cation, there are fewer symmetry operations relating equivalent organic molecules in the structure. Thus, compound **1** has only a single crystallographically distinct organic molecule, whereas **2** and **3** have two distinct molecules, and **4** has four different molecules. The alkyl ammonium tails of inequivalent molecules exhibit differences in length in compounds **2**, **3**, and **4**, as depicted in Figure 2.

This results in displacement of the molecules to different extents along the layer stacking axis, which likely occurs in order to accommodate close packing and beneficial van der Waals and/or electrostatic interactions between adjacent molecules in the double layer. It also reflects the more flexible conformation of the alkyl chains compared to the rigid phenyl ring. The asymmetric approach of inequivalent organic molecules to the inorganic layer also results in different hydrogen bonding patterns, which are shown in Figure S1. To retain effective hydrogen bond lengths between N−H···Cl−Mn, the six Mn−Cl bonds in an octahedron become unequal in **2**, **3**, and **4**; thus, the $MnCl_6$ octahedra are no longer perfectly regular (see Table S1). Furthermore, the in-plane Mn−Cl−Mn bond angles linking adjacent MCl_6 octahedra also deviate from 180°; the corresponding Glazer octahedral tilt systems are listed in Table 2, where we regard the stacking axis as c for the purposes of the notation. Table 2 lists the octahedral buckling angles of **1**−**4** as well as centrosymmetric $(CH_3NH_3)_2MnCl_4$ [$(MA)_2MnCl_4$] (ICSD 110654) and $(C_2H_5NH_3)_2MnCl_4$ [$(EA)_2MnCl_4$] (ICSD 110452) for comparison. The buckling angle is defined here as the angle between the line connecting the two apical chloride ions of an octahedron and the long unit cell axis. We note that a phase transition involving the onset of octahedral buckling breaks inversion symmetry and leads to ferroelectric order in

https://doi.org/10.1021/acs.inorgchem.1c01011
Inorg. Chem. 2021, 60, 15151−15158

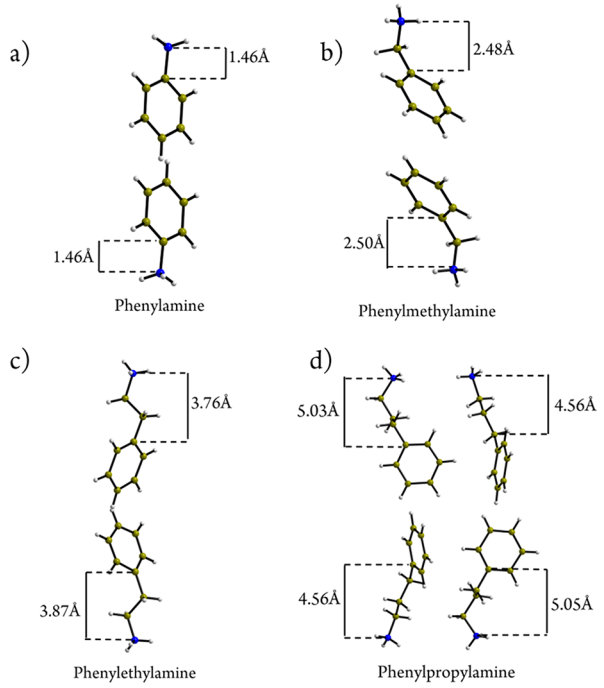

Figure 2. Lengths of alkyl-ammonium tails in adjacent organic cations in (a) $(PA)_2MnCl_4$, (b) $(PMA)_2MnCl_4$, (c) $(PEA)_2MnCl_4$, and (d) $(PPA)_2MnCl_4$.

Table 2. Buckling Angles and Mn^{2+} Off-Center Shifts for $MnCl_4$-Based Layered Perovskites Determined at 100 K

compd	space group	buckling angle (deg)	Mn^{2+} shift (pm)		Glazer tilt system
			a-axis	*c*-axis	
$(MA)_2MnCl_4$[33−35]	$P4_2/ncm$	7.3			$a^-a^0c^0$
$(EA)_2MnCl_4$[33,36,37]	*Pbca*	6.2			$a^-a^-c^0$
1, $(PA)_2MnCl_4$	$P2_1/c$	13.9			$a^-b^-c^0$
2, $(PMA)_2MnCl_4$	*Cc*	7.8	3.7	0.4	$a^+b^-c^0$
3, $(PEA)_2MnCl_4$	$Pca2_1$	6.9		0.8	$a^-b^-c^0$
4, $(PPA)_2MnCl_4$	*Pc*	2.7	11.2	1.0	$a^-b^-c^0$
		19.1	1.3	3.8	

$(PEA)_2CuCl_4$[15] via the onset of hydrogen bond order associated with rotation of the terminal NH_3 group of the PEA cation. However, in our current study buckling of the octahedra not only is observed in the polar structures of **2**, **3**, and **4**, but also is present in **1**. For **1**, effective hydrogen bonding can again only be preserved while simultaneously accommodating van der Waals interactions between the adjacent molecules in the double layer when the Mn^{2+} and Cl^- ions are slightly displaced, giving rise to buckling. Therefore, the case of $(PEA)_2CuCl_4$ appears to be an exception to the rule followed by **2**−**4** and other 2D perovskites with molecules containing phenyl or cycloalkane rings (see discussion below) where buckling of the metal halide octahedra is not the primary mechanism that breaks inversion symmetry.

Table 2 also lists the shifts of Mn^{2+} from the center of the octahedra, which we define as the weighted average coordinates of the 6 Cl^- ions. The components of the shifts along the polar axis are given for **2**−**4**, in-plane (*a*-axis) for **2** and **4**, and out-of-plane (*c*-axis) for **3**. For the centrosymmetric compounds, the shifts in the out-of-plane direction are given, which cancel by symmetry.

Single-crystal XRD shows that the centrosymmetric $P2_1/c$ structure of **1** is retained from 100 K up to at least 360 K, and that the polar *Cc* structure of **2** is retained up to at least 400 K (see Tables S2 and S3). No significant changes in the structures of **1** and **2** occur in this temperature range, other than an increase in the lattice parameters due to thermal expansion. This is also supported by room temperature powder XRD, the profiles of which were fitted reasonably well using the structural parameters obtained from single-crystal XRD (see Figure S2). In contrast, **3** undergoes two successive phase transitions above 100 K, first to a polar orthorhombic *Aea*2 phase at 363 K in which the organic cations become partially disordered and the buckling of the octahedra is removed, and then to a centrosymmetric tetragonal *I*4/*mmm* phase at 423 K (the decomposition temperature is ∼470 K) in which the cations are fully rotationally disordered.[17] In the case of **4**, the single-crystal XRD data collected at higher temperature were not of sufficient quality to obtain satisfactory structure solutions (the spots become strongly smeared, probably due to slight rotations of the layers); thus, the atomic coordinates determined by single-crystal XRD at 100 K were used to fit the powder XRD pattern in Figure S2d. The fit suggests that no phase transition occurs below room temperature. Differential scanning calorimetry (DSC) and thermal gravimetry (TG) measurements were also performed on **1**, **2**, and **4** over the temperature range 200−800 K and provided no evidence for any phase transitions below the decomposition temperatures of ∼380, ∼440, and ∼430 K, respectively (see Figures S3 and S4).

Inversion symmetry breaking has been reported in several other 2D perovskites with cations containing phenyl or cycloalkane rings. For example, $(PMA)_2PbCl_4$[38] adopts a high-temperature nonpolar (*Cmca*) state in which the organic cation exhibits 2-fold orientational disorder, and with decreasing temperature a polar transition occurs, below which only one of the two orientations is preserved (space group $Cmc2_1$). The same mechanism has been reported for a fluorinated phenyl ring in $(2FPMA)_2PbCl_4$ (*I*4/*mmm* to $Cmc2_1$ transition),[39] and for cycloalkane cations in $(CHA)_2PbBr_{4-x}I_x$ (CHA = cyclohexylammonium, *Cmca* to $Cmc2_1$ transition)[40] and $(CPA)_2CdBr_4$ (CPA = cyclopentylammonium, *Pnam* to $Pna2_1$ transition).[41] Polar structures have further been reported for $(PEA)_2SnI_4$ (space group *P*1),[42] $(PMA)_2PbBr_4$ (space group $Cmc2_1$),[43] and $(PEA)_2GeI_4$ (space group *P*1),[44] which might arise from the same structural considerations. A rotational order−disorder-type phase transition has also been reported for the butylammonium (C4A) cation in $(C4A)_2PbCl_4$ (*Cmca* to polar $Cmc2_1$),[45] and $(C5A)_2CuCl_4$ is reported to be polar (*Cc*) although it is unknown whether any phase transition occurs.[46]

Compounds **1**−**4** all show two-dimensional antiferromagnetic characteristics, with a broad maximum in the magnetic susceptibility versus temperature curve at ∼70−80 K (Figure 3 and Figure S5). For each compound, a sharp change in slope takes place in the range 42−46 K, suggesting the onset of three-dimensional order. Compound **1** shows a slightly higher susceptibility below the 3D ordering temperature (T_N) when the field is applied in-plane compared to out-of-plane, but the overall behavior is similar. In contrast, for compounds **2**, **3** and **4**, the susceptibility drops and approaches zero with decreasing temperature when measured out-of-plane, suggesting that the

https://doi.org/10.1021/acs.inorgchem.1c01011
Inorg. Chem. 2021, 60, 15151−15158

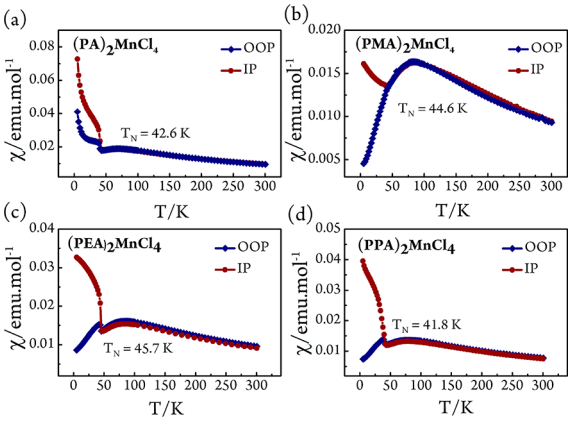

Figure 3. Magnetic susceptibility versus temperature for (a) $(PA)_2MnCl_4$, (b) $(PMA)_2MnCl_4$, (c) $(PEA)_2MnCl_4$, and (d) $(PPA)_2MnCl_4$, measured with a field of 1000 Oe applied along the in-plane (IP) and out-of-plane (OOP) directions.

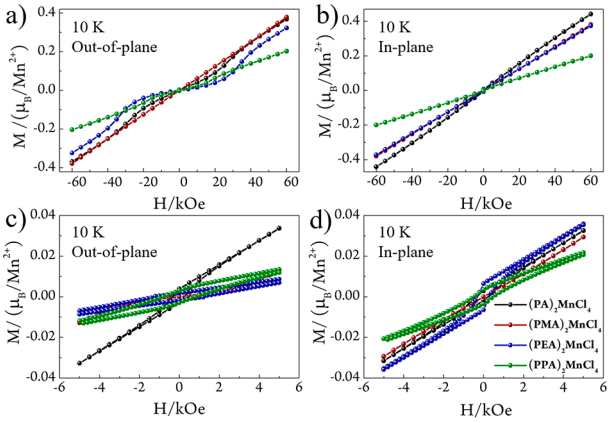

Figure 4. Field-dependent magnetization measured at 10 K in high and low magnetic fields along the (a, c) out-of-plane and (b, d) in-plane directions.

easy-axis lies in this direction. The susceptibility rises steeply when measured parallel to the inorganic layer, suggesting a ferromagnetic component as described in a previous report on $(PEA)_2MnCl_4$.[21] An ideal 2D Heisenberg antiferromagnet should not have a finite ordering temperature; however, in real magnetic systems, we cannot ignore weak exchange interactions in the perpendicular direction, as well as Ising anisotropy and/or Dzyaloshinski−Moriya (DM) interactions, all of which can lead to 3D ordering. It is known that the spins in 2D manganese halide perovskites are aligned in antiparallel fashion in-plane, and the weak ferromagnetism arises due to spin canting as a result of antisymmetric DM interactions associated with the tilted $MnCl_6$ octahedra.[22]

We observe that, besides the anisotropy at low temperature, the in-plane and out-of-plane susceptibility curves from ∼100 to 300 K lie almost perfectly on top of each other as expected for two-dimensional magnets (see Figure 3). Curie−Weiss fits to the inverse susceptibility data were performed in the range 150−300 K, and the extracted Weiss constants (θ) and effective magnetic moments (μ_{eff}) are given in Table 3. The Weiss constants are large and negative for all four compounds, confirming strong antiferromagnetic interactions. The effective moments are in the range 5.5−5.9 μ_B/Mn^{2+}, which is consistent with the expected spin-only value of 5.92 μ_B for the high-spin configuration of the Mn^{2+} ion. Field-dependent magnetization measurements were carried out to probe the weak ferromagnetism below the ordering temperature. As depicted in Figure 4, narrow hysteresis loops are apparent for **1**, **3**, and **4** when the applied field is in-plane. The magnetization then increases linearly at higher fields, consistent with the dominant antiferromagnetic component. The coercive field and remanent magnetization of the compounds are listed in Table 3, together with the spin canting angle α obtained from the relation $\sin \alpha = M_R/M_s$.

For the out-of-plane magnetization, we observe inflection points that might be related to a spin-flop transition as previously observed for $(PEA)_2MnCl_4$.[22] Spin-flop transitions in an antiferromagnet occur when a magnetic field perpendicular to the easy-axis causes the antiparallel spins to flop to the perpendicular direction. This critical magnetic field is known as the spin-flop field (H_{sf}),[47] which is also listed in Table 3.

We analyzed the 2D Heisenberg antiferromagnetism following Curély's work on square lattice antiferromagnets.[27,48−50] The equation below can be used to explain the temperature-dependent magnetic susceptibility of 2D antiferromagnets and is known to work well for the Mn^{2+} ion:

$$\chi = \frac{\beta G^2}{3}\left(\frac{1 + L(-\beta J)}{1 - L(-\beta J)}\right)^2 \quad (1)$$

Here, L, G, and J are the Langevin function, Landé factor, and exchange energy, respectively, and $\beta = 1/kT$ (k is the Boltzmann constant). Figure 5 shows corresponding fits to the susceptibility of **1**−**4**. Curély also derived an equation that allows us to estimate the theoretical temperature of maximum susceptibility, referred to as $T(\chi_{max})$, given by

$$\frac{kT(\chi_{max})}{JS(S+1)} = 1.2625 \quad (2)$$

Here $S = {}^5/_2$ for Mn^{2+}. Table 4 lists G, J, and both the theoretical and experimental values of $T(\chi_{max})$. Equations 1 and 2 have previously been used to explain the 2D antiferromagnetic characteristics of $(MA)_2MnCl_4$ and other $MnCl_4$-based layered perovskites with linear alkyl chains.[22,27] Here, we show that layered perovskites with arylamine-based ligands also retain similar 2D antiferromagnetic characteristics. The Landé factors are comparable to that of $(MA)_2MnCl_4$, reported as 1.89 μ_B/h.[27] The values of $T(\chi_{max})$ calculated using

Table 3. Magnetic Parameters of 1−4

compd	T_N (K)	θ (K)	μ_{eff} (μ_B)	H_{sf} (kOe)	$H_{Coercive}$ (Oe)	M_R (μ_B)	α (deg)
1, $(PA)_2MnCl_4$	42.6	−126	5.75	30	240	0.0036	0.036
2, $(PMA)_2MnCl_4$	44.6	−135	5.71	10			
3, $(PEA)_2MnCl_4$	45.7	−162	5.96	35	280	0.0033	0.032
4, $(PPA)_2MnCl_4$	41.8	−148	5.53	20	490	0.0028	0.029

https://doi.org/10.1021/acs.inorgchem.1c01011
Inorg. Chem. 2021, 60, 15151−15158

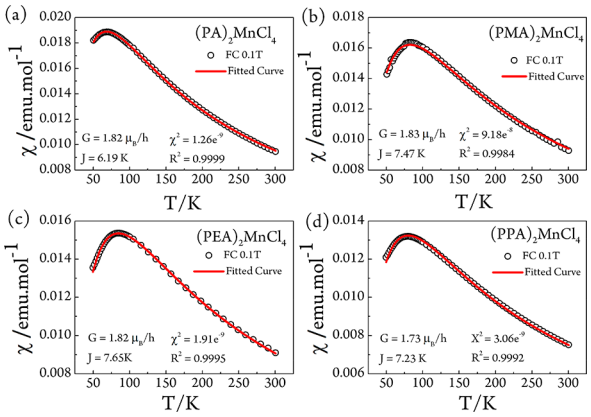

Figure 5. Temperature-dependent magnetic susceptibility along the in-plane direction of (a) $(PA)_2MnCl_4$, (b) $(PMA)_2MnCl_4$, (c) $(PEA)_2MnCl_4$, and (d) $(PPA)_2MnCl_4$, fitted using eq 1 (red line).

Table 4. Landé Factor, Exchange Energy, and Temperature of χ_{max}

compd	G (μ_B/h)	J/k_B (K)	$T(\chi_{max})_{Th}$ (K)	$T(\chi_{max})_{Exp}$ (K)
1, $(PA)_2MnCl_4$	1.82	6.19	68.4	68.4 ± 2
2, $(PMA)_2MnCl_4$	1.83	7.47	82.5	82.3 ± 2
3, $(PEA)_2MnCl_4$	1.82	7.65	85.4	84.3 ± 2
4, $(PPA)_2MnCl_4$	1.73	7.23	79.9	78.8 ± 2

eq 2 are close to those obtained experimentally (Table 4), confirming that all four compounds exhibit 2D-Heisenberg antiferromagnetic behavior above the Néel temperature. This is consistent with our observation that the magnetic parameters do not show any obvious dependence on the cation length (Table S4).

CONCLUSIONS

We report three new $MnCl_4$-based layered inorganic−organic perovskite compounds containing the arylamine cations PA, PMA, and PPA, and we compare their properties with those of the previously studied analogue containing the PEA cation. We show that the presence of an alkyl tail of at least one carbon atom is important to obtain a polar crystal structure. We suggest that the rotational degree of freedom of such organic cations is an important factor that can give rise to the breaking of inversion symmetry. To achieve beneficial van der Waals and/or electrostatic interactions, adjacent organic molecules arrange themselves such that the flexible alkyl tails have different lengths when approaching the inorganic layer. This gives rise to different hydrogen bonding patterns between the organic and inorganic layers, which also result in buckled MCl_6 octahedra. The buckling of the MCl_6 octahedra does not itself govern the presence of a polar structure. For $(PMA)_2MnCl_4$ and $(PPA)_2MnCl_4$, the polar structure is stable up to the decomposition temperature. We observe 2D antiferromagnetism in all four compounds, manifested by a broad maximum in the magnetic susceptibility in the range ∼70−80 K that can be fitted by the 2D Heisenberg model of Curély. All samples show the presence of a weak ferromagnetic component below the long-range ordering temperature of 42−46 K due to spin canting.

ASSOCIATED CONTENT

Supporting Information

The Supporting Information is available free of charge at https://pubs.acs.org/doi/10.1021/acs.inorgchem.1c01011.

Crystallographic data and structural refinement parameters, hydrogen bonding patterns, powder XRD fits, unit cell parameters at various temperatures for $(PA)_2MnCl_4$ and $(PMA)_2MnCl_4$, DSC and TGA data for all samples, and temperature- and field-dependent magnetization of all samples measured along the in-plane and out-of-plane directions (PDF)

Accession Codes

CCDC 2074096−2074098 contain the supplementary crystallographic data for this paper. These data can be obtained free of charge via www.ccdc.cam.ac.uk/data_request/cif, or by emailing data_request@ccdc.cam.ac.uk, or by contacting The Cambridge Crystallographic Data Centre, 12 Union Road, Cambridge CB2 1EZ, UK; fax: +44 1223 336033.

AUTHOR INFORMATION

Corresponding Author

Graeme R. Blake − *Zernike Institute for Advanced Materials, University of Groningen, 9747AG Groningen, Netherlands;* orcid.org/0000-0001-9531-7649; Email: g.r.blake@rug.nl

Authors

Liany Septiany − *Zernike Institute for Advanced Materials, University of Groningen, 9747AG Groningen, Netherlands*

Diana Tulip − *Zernike Institute for Advanced Materials, University of Groningen, 9747AG Groningen, Netherlands*

Mikhail Chislov − *Institute of Chemistry, Department of Chemical Thermodynamics and Kinetics, Center for Thermal Analysis and Calorimetry, St. Petersburg State University, 198504 Peterhof, Russia*

Jacob Baas − *Zernike Institute for Advanced Materials, University of Groningen, 9747AG Groningen, Netherlands*

Complete contact information is available at: https://pubs.acs.org/10.1021/acs.inorgchem.1c01011

Notes

The authors declare no competing financial interest.

ACKNOWLEDGMENTS

L.S. thanks the Indonesian Endowment Fund for Education (LPDP) for supporting her PhD study.

REFERENCES

(1) Grancini, G.; Nazeeruddin, M. K. Dimensional Tailoring of Hybrid Perovskites for Photovoltaics. *Nat. Rev. Mater.* **2019**, *4* (1), 4−22.

(2) Stoumpos, C. C.; Malliakas, C. D.; Kanatzidis, M. G. Semiconducting Tin and Lead Iodide Perovskites with Organic Cations: Phase Transitions, High Mobilities, and Near-Infrared Photoluminescent Properties. *Inorg. Chem.* **2013**, *52* (15), 9019−9038.

(3) Wang, H.; Fang, C.; Luo, H.; Li, D. Recent Progress of the Optoelectronic Properties of 2D Ruddlesden-Popper Perovskites. *J. Semicond.* **2019**, *40* (4), 041901.

(4) Pedesseau, L.; Sapori, D.; Traore, B.; Robles, R.; Fang, H. H.; Loi, M. A.; Tsai, H.; Nie, W.; Blancon, J. C.; Neukirch, A.; Tretiak, S.; Mohite, A. D.; Katan, C.; Even, J.; Kepenekian, M. Advances and

Promises of Layered Halide Hybrid Perovskite Semiconductors. *ACS Nano* **2016**, *10* (11), 9776−9786.
(5) Cheng, Z.; Lin, J. Layered Organic-Inorganic Hybrid Perovskites: Structure, Optical Properties, Film Preparation, Patterning and Templating Engineering. *CrystEngComm* **2010**, *12* (10), 2646−2662.
(6) de Jongh, L. J.; Miedema, A. R. Experiments on Simple Magnetic Model Systems. *Adv. Phys.* **1974**, *23*, 1−260.
(7) Ma, Y.; Zhai, K.; Yan, L.; Chai, Y.; Shang, D.; Sun, Y. Magnetocaloric Effect in the Layered Organic-Inorganic Hybrid $(CH_3NH_3)_2CuCl_4$. *Chin. Phys. B* **2018**, *27*, 027501.
(8) Bochalya, M.; Kumar, S. Magnetocaloric Effect in 2D-Alkylammonium Copper Halides Layered Inorganic-Organic Systems. *J. Appl. Phys.* **2020**, *127*, 055501.
(9) Pandey, R.; Vats, G.; Yun, J.; Bowen, C. R.; Ho-Baillie, A. W. Y.; Seidel, J.; Butler, K. T.; Seok, S. I. Mutual Insight on Ferroelectrics and Hybrid Halide Perovskites: A Platform for Future Multifunctional Energy Conversion. *Adv. Mater.* **2019**, *31*, 1807376.
(10) Shahrokhi, S.; Gao, W.; Wang, Y.; Anandan, P. R.; Rahaman, M. Z.; Singh, S.; Wang, D.; Cazorla, C.; Yuan, G.; Liu, J. M.; Wu, T. Emergence of Ferroelectricity in Halide Perovskites. *Small Methods* **2020**, *4* (8), 2000149.
(11) Nandi, P.; Topwal, D.; Park, N.-G.; Shin, H. Organic-Inorganic Hybrid Lead Halides as Absorbers in Perovskite Solar Cells: A Debate on Ferroelectricity. *J. Phys. D: Appl. Phys.* **2020**, *53* (49), 493002.
(12) Spaldin, N. A.; Ramesh, R. Advances in Magnetoelectric Multiferroics. *Nat. Mater.* **2019**, *18* (3), 203−212.
(13) Eerenstein, W.; Mathur, N. D.; Scott, J. F. Multiferroic and Magnetoelectric Materials. *Nature* **2006**, *442* (7104), 759−765.
(14) Khomskii, D. Classifying Multiferroics: Mechanisms and Effects. *Physics (College. Park. Md).* **2009**, *2*, 20.
(15) Polyakov, A. O.; Arkenbout, A. H.; Baas, J.; Blake, G. R.; Meetsma, A.; Caretta, A.; Van Loosdrecht, P. H. M.; Palstra, T. T. M. Coexisting Ferromagnetic and Ferroelectric Order in a CuCl4-Based Organic-Inorganic Hybrid. *Chem. Mater.* **2012**, *24*, 133−139.
(16) Huang, B.; Wang, B. Y.; Du, Z. Y.; Xue, W.; Xu, W. J.; Su, Y. J.; Zhang, W. X.; Zeng, M. H.; Chen, X. M. Importing Spontaneous Polarization into a Heisenberg Ferromagnet for a Potential Single-Phase Multiferroic. *J. Mater. Chem. C* **2016**, *4* (37), 8704−8710.
(17) Kamminga, M. E.; Hidayat, R.; Baas, J.; Blake, G. R.; Palstra, T. T. M. Out-of-Plane Polarization in a Layered Manganese Chloride Hybrid. *APL Mater.* **2018**, *6* (6), 066106.
(18) Willett, R. D.; Gómez-García, C. J.; Twamley, B. Long-Range Order in Layered Perovskite Salts - Structure and Magnetic Properties of $[(CH3)_2CHCH_2NH_3]_2CuX_4$ (X = Cl, Br). *Eur. J. Inorg. Chem.* **2012**, *2012* (20), 3342−3348.
(19) Dupas, A.; Le Dang, K.; Renard, J. P.; Veillet, P.; Daoud, A.; Perret, R. Magnetic Properties of the Nearly Two-Dimensional Ferromagnets $[C_6H_5(CH_2)_nNH_3]_2CuCl_4$ with n = 1,2,3. *J. Chem. Phys.* **1976**, *65*, 4099−4102.
(20) Huang, B.; Zhang, J. Y.; Huang, R. K.; Chen, M. K.; Xue, W.; Zhang, W. X.; Zeng, M. H.; Chen, X. M. Spin-Reorientation-Induced Magnetodielectric Coupling Effects in Two Layered Perovskite Magnets. *Chem. Sci.* **2018**, *9* (37), 7413−7418.
(21) Park, S.-H.; Oh, I.-H.; Park, S.; Park, Y.; Kim, J. H.; Huh, Y.-D. Canted Antiferromagnetism and Spin Reorientation Transition in Layered Inorganic-Organic Perovskite $(C_6H_5CH_2CH_2NH_3)_2MnCl_4$. *Dalt. Trans.* **2012**, *41* (4), 1237−1242.
(22) Lee, K. W.; Lee, C. H.; Lee, C. E.; Kang, J. Magnetic Ordering in Two-Dimensional Heisenberg Antiferromagnets with Variable Interlayer Distances. *Phys. Rev. B: Condens. Matter Mater. Phys.* **2000**, *62* (1), 95−98.
(23) Heger, G.; Henrich, E.; Kanellakopulos, B. Investigations of a Quasi Two-Dimensional Heisenberg Antiferromagnetic System. Nondeuterated and Deuterated Alkyl-Ammonium-Tetrachloromanganate. *Solid State Commun.* **1973**, *12* (11), 1157−1165.
(24) van Amstel, W. D.; de Jongh, L. J. Magnetic Measurements on $(CH_3NH_3)_2MnCI_4$, a Quasi Two-Dimensional Heisenberg Antiferromagnet. *Solid State Commun.* **1972**, *11*, 1423−1429.
(25) Nakajima, T.; Yamauchi, H.; Goto, T.; Yoshizawa, M.; Suzuki, T.; Fujimura, T. Magnetic and Elastic Properties of $(CH_3NH_3)_2FeCl_4$ and $(C_2H_5NH_3)_2FeCl_4$. *J. Magn. Magn. Mater.* **1983**, *31*−*34*, 1189−1190.
(26) Han, J.; Nishihara, S.; Inoue, K.; Kurmoo, M. High Magnetic Hardness for the Canted Antiferromagnetic, Ferroelectric, and Ferroelastic Layered Perovskite-like $(C_2H_5NH_3)_2[Fe^{II}Cl_4]$. *Inorg. Chem.* **2015**, *54* (6), 2866−2874.
(27) Curély, J.; Rouch, J. Thermodynamics of the 2D-Heisenberg Classical Square Lattice Part III. Study of the Static Susceptibility Behaviours. *Phys. B* **1998**, *254* (3−4), 298−321.
(28) Sheldrick, G. M. A Short History of SHELX. *Acta Crystallogr., Sect. A: Found. Crystallogr.* **2008**, *64*, 112−122.
(29) Toby, B. H.; Von Dreele, R. B. GSAS-II: The Genesis of a Modern Open-Source All Purpose Crystallography Software Package. *J. Appl. Crystallogr.* **2013**, *46*, 544−549.
(30) Heger, G.; Mullen, D.; Knorr, K. On the Second-Order Phase Transition in $(CH_3NH_3)_2MnCl_4$. *Phys. Stat. Sol A* **1975**, *31*, 455−462.
(31) Sakami, T.; Ohtani, T.; Matsumoto, Y.; Ochi, D.; Xi, X.; Kamikawa, S.; Ohyama, J.; Ishii, I.; Suzuki, T. Successive Phase Transitions in Single-Crystalline $(C_2H_5NH_3)_2CuCl_4$ and Potential of Multiferroicity. *Solid State Commun.* **2019**, *290*, 49−54.
(32) Arend, H.; Hofmann, R.; Waldner, F. New Phase Transition in $(C_nH_{2n+1}NH_3)_2MnCl_4$. *Solid State Commun.* **1973**, *13* (10), 1629−1632.
(33) Depmeier, W.; Felsche, J.; Wildermuth, G. Phases and Phase Transitions of Compounds $(C_nH_{2n+1}NH_3)_2MnCl_4$ with n = 1, 2, 3. *J. Solid State Chem.* **1977**, *21* (1), 57−65.
(34) Aleksandrov, K. S.; Bartolome, J. Octahedral Tilt Phases in Perovskite-like Crystals with Slabs Containing an Even Number of Octahedral Layers. *J. Phys.: Condens. Matter* **1994**, *6* (40), 8219−8235.
(35) Heger, G.; Mullen, D.; Knorr, K. On the Importance of Hydrogen Bonding for the Structural Phase Transitions in $(CH_3NH_3)_2MnCl_4$. *Phys. Stat. Sol A* **1976**, *35*, 627−637.
(36) Brunskill, I. H.; Depmeier, W. The Layered Perovskites $(C_3H_7NH_3)_2MnCl_4$ (PAMC) and $(C_2H_5NH_3)_2MnCl_4$ (EAMC): Birefringence Studies and the Symmetry of the Commensurately Modulated ϵ Phase of PAMC. *Acta Crystallogr., Sect. A: Cryst. Phys., Diffr., Theor. Gen. Crystallogr.* **1982**, *A38* (1), 132−137.
(37) Depmeier, W. The Crystal Structure of γ-Bis(Ethylammonium) Tetrachloromanganate(II) at 126 K and Its Phase Transition. *Acta Crystallogr., Sect. B: Struct. Crystallogr. Cryst. Chem.* **1977**, *B33* (12), 3713−3718.
(38) Liao, W. Q.; Zhang, Y.; Hu, C. L.; Mao, J. G.; Ye, H. Y.; Li, P. F.; Huang, S. D.; Xiong, R. G. A Lead-Halide Perovskite Molecular Ferroelectric Semiconductor. *Nat. Commun.* **2015**, *6*, 7338.
(39) Shi, P. P.; Lu, S. Q.; Song, X. J.; Chen, X. G.; Liao, W. Q.; Li, P. F.; Tang, Y. Y.; Xiong, R. G. Two-Dimensional Organic-Inorganic Perovskite Ferroelectric Semiconductors with Fluorinated Aromatic Spacers. *J. Am. Chem. Soc.* **2019**, *141* (45), 18334−18340.
(40) Ye, H. Y.; Liao, W. Q.; Hu, C. L.; Zhang, Y.; You, Y. M.; Mao, J. G.; Li, P. F.; Xiong, R. G. Bandgap Engineering of Lead-Halide Perovskite-Type Ferroelectrics. *Adv. Mater.* **2016**, *28* (13), 2579−2586.
(41) Huang, C. R.; Luo, X.; Liao, W. Q.; Tang, Y. Y.; Xiong, R. G. An Above-Room-Temperature Molecular Ferroelectric: [Cyclopentylammonium]$_2CdBr_4$. *Inorg. Chem.* **2020**, *59* (1), 829−836.
(42) Gao, Y.; Wei, Z.; Yoo, P.; Shi, E.; Zeller, M.; Zhu, C.; Liao, P.; Dou, L. Highly Stable Lead-Free Perovskite Field-Effect Transistors Incorporating Linear Π-Conjugated Organic Ligands. *J. Am. Chem. Soc.* **2019**, *141* (39), 15577−15585.
(43) Du, K. Z.; Tu, Q.; Zhang, X.; Han, Q.; Liu, J.; Zauscher, S.; Mitzi, D. B. Two-Dimensional Lead(II) Halide-Based Hybrid Perovskites Templated by Acene Alkylamines: Crystal Structures, Optical Properties, and Piezoelectricity. *Inorg. Chem.* **2017**, *56* (15), 9291−9302.
(44) Cheng, P.; Wu, T.; Zhang, J.; Li, Y.; Liu, J.; Jiang, L.; Mao, X.; Lu, R. F.; Deng, W. Q.; Han, K. (C6H5C2H4NH3)2GeI4: A Layered

https://doi.org/10.1021/acs.inorgchem.1c01011
Inorg. Chem. 2021, 60, 15151−15158

Two-Dimensional Perovskite with Potential for Photovoltaic Applications. *J. Phys. Chem. Lett.* **2017**, *8* (18), 4402−4406.
(45) Ji, C.; Wang, S.; Li, L.; Sun, Z.; Hong, M.; Luo, J. The First 2D Hybrid Perovskite Ferroelectric Showing Broadband White-Light Emission with High Color Rendering Index. *Adv. Funct. Mater.* **2019**, *29* (6), 1805038.
(46) Willett, R.; Place, H.; Middleton, M. Crystal Structures of Three New Copper(II) Halide Layered Perovskites: Structural, Crystallographic, and Magnetic Correlations. *J. Am. Chem. Soc.* **1988**, *110* (26), 8639−8650.
(47) Wang, X. Y.; Wang, L.; Wang, Z. M.; Su, G.; Gao, S. Coexistence of Spin-Canting, Metamagnetism, and Spin-Flop in a (4,4) Layered Manganese Azide Polymer. *Chem. Mater.* **2005**, *17* (25), 6369−6380.
(48) Curély, J. Thermodynamics of the 2D-Heisenberg Classical Square Lattice: Zero-Field Partition Function. *Phys. B* **1998**, *245* (3), 263−276.
(49) Curély, J. Thermodynamics of the 2D-Heisenberg Classical Square Lattice Part II. Thermodynamic Functions Derived from the Zero-Field Partition Function. *Phys. B* **1998**, *254* (3−4), 277−297.
(50) Curély, J.; Kliava, J. Magnetism of 2d Heisenberg Classical Square Lattices: Theory vs Experiments. *Phys. Stat. Solidi C* **2014**, *11* (5−6), 989−994.

https://doi.org/10.1021/acs.inorgchem.1c01011
Inorg. Chem. 2021, 60, 15151−15158